Ultrastrong Coupling of Band-Nested Excitons in Few-Layer Molybdenum Disulphide

Aaron H. Rose,* Taylor J. Aubry, Hanyu Zhang, and Jao van de Lagemaat*

The 2D transition-metal dichalcogenides (2D TMDCs) are an intriguing platform for studying strong light–matter interactions because they combine the electronic properties of conventional semiconductors with the optical resonances found in organic systems. However, the coupling strengths demonstrated in strong exciton–polariton coupling in the 2D TMDCs remain much lower than those found in organic systems. In this paper, a new approach is taken by utilizing the large oscillator strength of the above-band gap C exciton in few-layer molybdenum disulphide (FL-MoS$_2$). A k-space Rabi splitting of 293 meV is shown when coupling FL-MoS$_2$ C excitons to surface plasmon polaritons at room temperature. This value is 11% of the uncoupled exciton energy (2.67 eV or 464 nm), ≈2× what is typically seen in the TMDCs, placing the system in the ultrastrong coupling regime. The results take a step toward finally achieving the efficient quantum coherent processes of ultrastrong coupling in a CMOS-compatible system—the 2D TMDCs—in the visible spectrum.

1. Introduction

1.1. Strong Coupling and the 2D TMDCs

2D transition-metal dichalcogenides (TMDCs) have intriguing optical, electronic, and catalytic properties.[1–3] Their absorption is characterized by sharp excitonic resonances, making the TMDCs good candidates for strong exciton–polariton coupling.[4] In fact, one of the most exciting results in exciton–polariton systems—polariton condensation and lasing[5–7]—has recently been demonstrated in the TMDCs.[8–10] However, coupling strengths have remained much lower than what is achiev-

able in organic systems, with typical Rabi splitting values of ≲150 meV or ≲6% of the exciton energy. In organic systems, Rabi splitting of >10%, which is in the ultrastrong coupling regime, is common.[11–18] In the ultrastrong coupling regime, coupling interactions are expected to be more efficient and emergent quantum coherent phenomena, such as ground-state virtual photons and entangled pairs, are predicted to exist even at room temperature or without resolvable Rabi splitting due to broad resonators.[19,20] As such, it is desirable to achieve this regime in a CMOS-compatible system like the TMDCs. In this paper, we exploit the large oscillator strength of the C exciton in few-layer molybdenum disulphide (FL-MoS$_2$) to achieve ultrastrong coupling at room temperature.

1.2. The C Exciton of 2D TMDCs has Unique Properties

The C exciton of the 2D TMDCs does not arise from the same type of band structure features as the more commonly studied A and B excitons near the band edge, and thus, it has unique behavior. The A and B exciton absorption features in FL-MoS$_2$ are labeled in **Figure 1**a. These excitons correspond to transitions between the conduction band minimum and the spin–orbit-split valence band maxima at the K point in Figure 1b. The next prominent absorption feature is the C exciton, which has significantly larger oscillator strength than the A or B, as seen by comparing the Lorentzian fits in Figure 1a.

Interestingly, the C exciton does not arise from transitions between two opposite concavity parabolic bands, but rather between regions of parallel bands, referred to as nested bands, shown by the shaded region in Figure 1b.[21] The C exciton oscillator strength is large because of this parallel band region of k-space, and thus, the density of states at the C exciton transition energy is large.

An unusual consequence of the nested bands is that C exciton carriers are expected to spontaneously self-separate in momentum space[22–24] and exhibit slowed hot carrier cooling relative to the A and B excitons.[23] This slowed cooling has been seen by Wang et al.[23] and ourselves[25] in ultrafast spectroscopic studies. Typically, photoexcited hot carriers in semiconductor devices thermalize to the band edges on femtosecond timescales before reaching the contacts. Photovoltage is therefore limited to the bandgap potential. In contrast, for hot carrier devices,

A. H. Rose, T. J. Aubry, H. Zhang,[+] J. van de Lagemaat
National Renewable Energy Laboratory
Chemistry and Nanoscience Center
15013 Denver W Pkwy, Golden, CO 80401, USA
E-mail: aaron.rose@nrel.gov; jao.vandelagemaat@nrel.gov

The ORCID identification number(s) for the author(s) of this article can be found under https://doi.org/10.1002/adom.202200485.

[+]Present address: First Solar, 1035 Walsh Ave, Santa Clara, CA, 95050, USA

**ADVANCED
SCIENCE NEWS**

www.advancedsciencenews.com

**ADVANCED
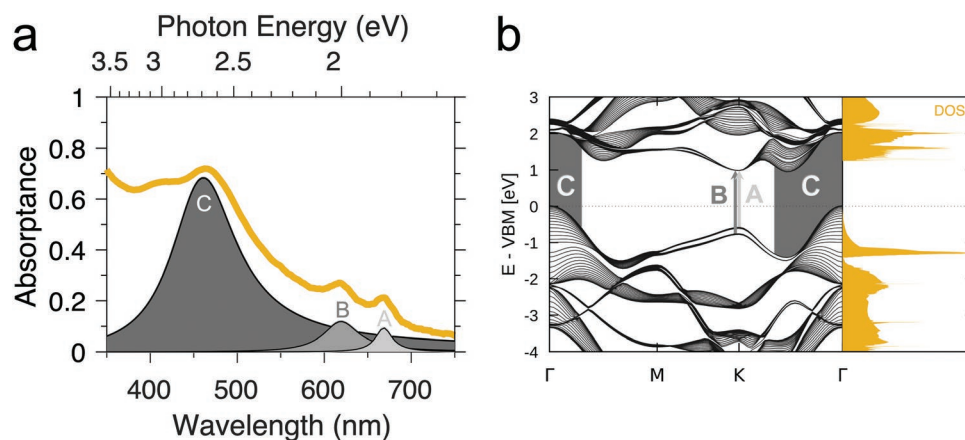OPTICAL
MATERIALS**

www.advopticalmat.de

Figure 1. a) Absorptance, A, of FL-MoS$_2$ film on 40 nm Ag on glass. Reflectance, R, of the film was taken and A calculated as $A = 1 - R$, where transmission is assumed to be negligible. b) Band structure and density of states of FL-MoS$_2$ (17 layers), predicted from density functional theory. The arrows labeled A and B point out A and B exciton transitions while the shaded region labeled C shows the nested band region where C exciton transitions may be excited.

charge extraction occurs faster than thermalization, and photovoltage is, therefore, limited to the photon potential. Wang et al. took advantage of the slow cooling of excited C exciton states to achieve 80% charge extraction efficiency from the C exciton in MoS$_2$–graphene heterostructures, showing the potential for harvesting hot carriers. In our previous work analyzing the kinetics of the ultrastrong coupling described here, we showed increased lifetimes of the two slowest C exciton decay processes by factors of 1.5 and 5.8.[25] Ultrastrong coupling of the C exciton in the TMDCs, therefore, may enhance hot carrier utilization for more efficient photovoltaic or photoelectrochemical energy conversion.

Another intriguing demonstration of C exciton physics in the TMDCs is the 400-fold enhancement of second harmonic generation (SHG) from the C exciton in monolayer WS$_2$ when weakly coupled to surface plasmon polaritons (SPPs).[26] Strong coupling has also been used to enhance SHG in organics and TMDCs while also modifying the emission spectra via Rabi splitting.[27,28] Thus, as ultrastrong coupling at the C exciton in MoS$_2$ prolongs carrier lifetimes,[25] it may offer a way to further tune and enhance the SHG, as well as other non-linear properties in the TMDCs.

Here, we study the steady-state optical properties of the C exciton in MoS$_2$ under ultrastrong coupling and model the experimental observations using transfer matrix simulations and the semiclassical coupled harmonic oscillator model. We show that we may take advantage of the large oscillator strength of the C exciton to increase the exciton–plasmon polariton coupling strength relative to the A and B excitons. We find that the enhancement pushes the coupling strength into the ultrastrong coupling regime, opening up the possibility to use the TMDCs as a CMOS-compatible platform for ultrastrong coupling studies in the visible spectrum.

2. Analysis in k-Space

2.1. Experimental Exciton–Plasmon Dispersion

We use the Kretschmann–Raether technique shown in **Figure 2**a to measure the p-polarized angle-resolved reflectance

spectrum, $R(\theta)$, and calculate the experimental dispersion of Figure 2b. Absorptance, $A(\theta)$, is calculated as $A(\theta) = 1 - R(\theta)$, where transmission is negligible under the total internal reflection conditions. A 40 nm Ag thin film coating the prism supports propagating surface plasmons that are excited through the backside of the prism (see Figure S2f, Supporting Information, for an example of the bare Ag plasmon dispersion). We transfer ≈10 nm FL-MoS$_2$ grown by chemical vapor deposition (CVD) onto the Ag to complete the samples. Finally, we convert the angle space, $A(\theta)$, dispersion into the more physically relevant[29] wavevector-space, $A(k_{//})$, by $k_{//} = (2\pi/\lambda)n\sin\theta_i$, where n is the wavelength-dependent lossless refractive index of the prism and θ_i is the angle of incidence within the glass prism.

Compared to our earlier work showing strong coupling at the A and B excitons in thicker MoS$_2$,[30] the features near the A and B excitons show only slight perturbations to the plasmon dispersion, indicating minimal coupling to these excitons (see Figure S1, Supporting Information, for dispersion showing the A and B excitons near 1.85 and 2 eV). However, at the C exciton position of 2.67 eV, a large Rabi splitting and avoided crossing is observed, indicating strong coupling. There is minimal overlap of two coupled modes labeled upper polariton (UP) and lower polariton (LP) due to the large splitting. We characterize the magnitude of the splitting in Section 2.3.

2.2. Simulated Exciton–Plasmon Dispersion

We performed transfer matrix model (TMM) simulations[31] of the observed dispersion in order to derive inputs for the semiclassical coupled harmonic oscillator model used in the next section. Specifically, once we have a good TMM fit to the data, we can modify that model to simulate the bare plasmon, which is a necessary input for the coupled oscillator model (see the next section and Supporting Information for more details). The simulated system, shown in Figure 2c, reproduces the experimental data well, and thus, can be used to design future
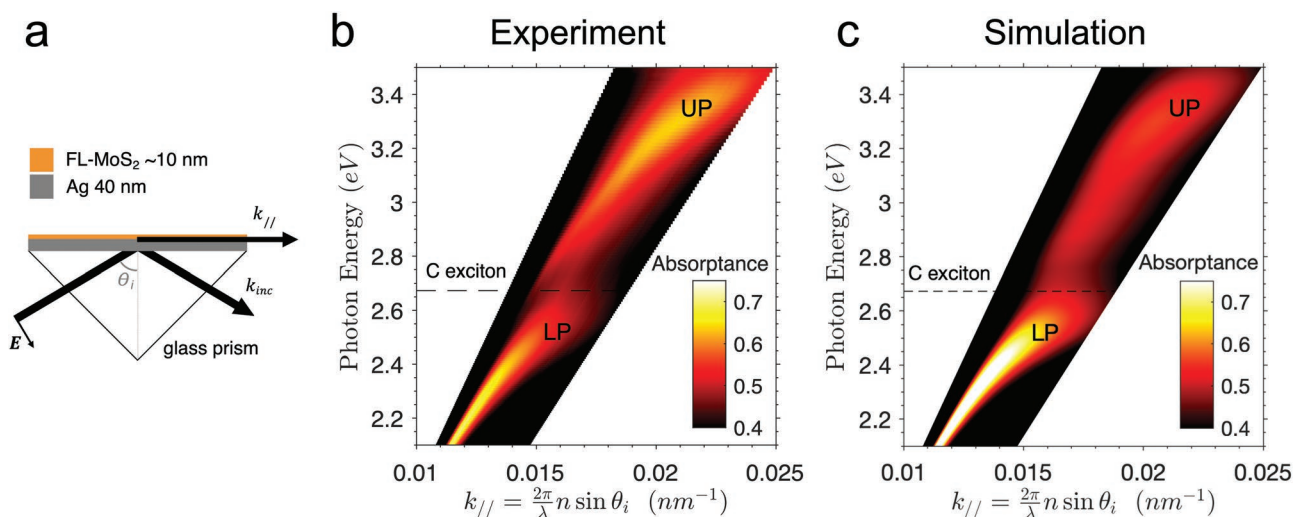
**ADVANCED
SCIENCE NEWS**
www.advancedsciencenews.com

**ADVANCED
OPTICAL
MATERIALS**
www.advopticalmat.de

Figure 2. a) Kretschmann–Raether method of measuring angle-resolved dispersion. P-polarized light is incident on the Ag–MoS₂ film through the bottom of the prism. The surface plasmon polariton propagates in the direction of $k_{//}$. b) Experimental dispersion. c) Transfer matrix model of the experimental dispersion. In (b) and (c), the upper polariton (UP) and lower polariton (LP) branches are labeled while the dashed line indicates the position of the uncoupled C exciton energy.

experiments, for example, photoelectrochemistry studies in a liquid electrolyte, which we know shifts the plasmon and requires a judicious choice of optical glass for the prism. The optical constants (see Figure S2a, Supporting Information) and thickness (10 nm) of our MoS₂ film were modeled from spectroscopic ellipsometry data, taken on the top (MoS₂) side of the prism. We know from our previous study[30] that thickness values extracted from ellipsometry closely align with those measured with atomic force microscopy and are further corroborated by photoluminescence and Raman measurements that indicate few-layer films. The optical constants were fed into the transfer matrix simulations and the thickness was fit to reproduce the experimental data. The simulation fit value for the MoS₂ thickness was 8 nm, near the value measured by ellipsometry of 10 nm.

In our previous study, we used ≈15 nm MoS₂ to achieve strong coupling at the A and B excitons.[30] In that case, the additional thickness served to red shift the plasmon dispersion so that its maximum energy lay below the C exciton energy. Thus, no coupling to the C exciton was observed as the two modes did not overlap. Furthermore, as the maximum plasmon energy approaches the exciton energies (while still overlapping them), the coupling strength increases.[32] In the current study, the thickness is, therefore, tuned for coupling to the C exciton.

2.3. Semiclassical Coupled Harmonic Oscillator Model

The transfer matrix simulations serve to verify that our observations are to be expected based on applying Maxwell's equations to the system at hand. However, they do not quantify the strength of the coupling or the composition of the new hybrid modes. To gain this insight, we solve the problem using a semiclassical coupled harmonic oscillator model. The Hamiltonian of the system can be written as in Equation (1)

$$
\begin{bmatrix}
E_{SPP}(k_{//}) & \dfrac{\Omega_A}{2} & \dfrac{\Omega_B}{2} & \dfrac{\Omega_C}{2} \\[2mm]
\dfrac{\Omega_A}{2} & E_A & 0 & 0 \\[2mm]
\dfrac{\Omega_B}{2} & 0 & E_B & 0 \\[2mm]
\dfrac{\Omega_C}{2} & 0 & 0 & E_C
\end{bmatrix}
\tag{1}
$$

In this model, the problem is treated as a four-level quantum system coupled to classical electromagnetic fields. $E_{SPP}(k_{//})$ is the uncoupled or "bare" plasmon energy, which is a function of the in-plane wave vector as given by its dispersion (discussed below). E_A, E_B, and E_C are the bare exciton energies. Ω_A, Ω_B, and Ω_C are the Rabi splitting values. The off-diagonal zeros represent that there is no coupling between excitons, which is expected to be the case. The Hamiltonian is solved and the eigenvalues give the four coupled modes. The two relevant modes in the region of the C exciton are shown as yellow lines in **Figure 3** (see Figure S3, Supporting Information, for all four modes). The model is fit by the least squares routine at each k-point to the experimental data. The experimental data, plotted in black in Figure 3, is represented by the peak energies found from fitting each branch of the dispersion to Lorentzians at each k-point.

E_A, E_B, and E_C are set as fit parameters, with initial values taken from the positions of the absorptance peaks in Figure 1a. Ω_A, Ω_B, and Ω_C are also set as fit parameters. Initial values of Ω are found by subtracting the energy of the branches on either side of each exciton and taking the minimum difference.

$E_{SPP}(k_{//})$ is not set as a fitting parameter, but is instead an approximated input to the model. Plasmons are sensitive to their local environment, defined by the near-field of the electromagnetic plasmon wave, ≈10–100 nm. Therefore, determining the bare plasmon energy, $E_{SPP}(k_{//})$, shown by the gray line in Figure 3, is more complicated than simply measuring
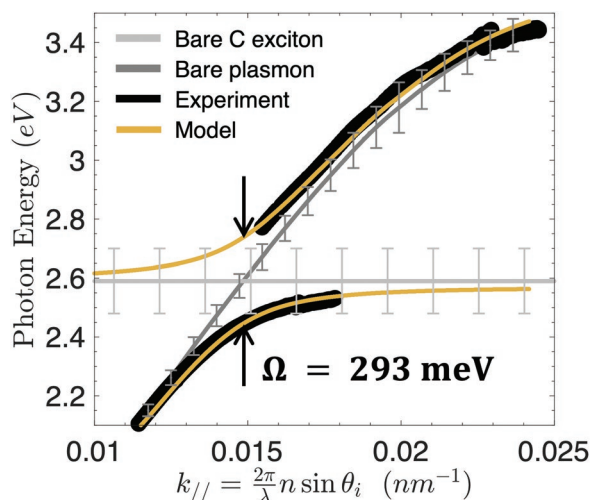
Figure 3. Coupled oscillator model fit to data. Black data points are from peaks in experimental UP and LP data in Figure 2b. The dark gray line is the peak fit of the simulated bare plasmon, $E_{SPP}(k_{//})$; error bars represent the fit Lorentzian width. Yellow lines are coupled oscillator model fits to the data. The light gray line is a fit to the C exciton energy position; error bars represent the fit Lorentzian width of the bare C exciton in k-space. The best fit value of the Rabi splitting is $\Omega = 293$ meV or 11% of splitting energy, indicating the ultrastrong coupling regime.
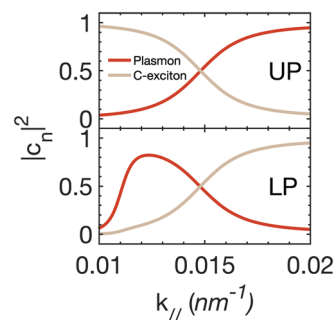

Figure 4. Hopfield/weighting coefficients of coupled modes in terms of uncoupled modes, taken from semiclassical oscillator model fit to experimental data. Here we focus on the two branches, UP and LP, of the coupled C exciton. See Figure S4, Supporting Information, for the coefficients of all four branches.

the dispersion of a control Ag sample with no MoS_2. The presence of several nanometers of any material, lossy or not, will modify the plasmon dispersion. In this case with MoS_2 on Ag, the plasmon asymptotically approaches ≈3.5 eV, which is red-shifted from the bare Ag case. Here, we approximate the bare plasmon with a fictitious lossless MoS_2 (see Supporting Information for further details). The bare plasmon dispersion is then fit to a Lorentzian at every k–point and the peak positions comprise $E_{SPP}(k_{//})$. The simulated bare plasmon overlaps well with the experimental data far from the point of maximum strong coupling, indicating a good approximation. Once we have the Hamiltonian inputs, we run the fitting routine and find that the fit matches the experimental data well, as seen in Figure 3. The results will be discussed after the next section.

2.4. Hybridization Coefficients in k-Space

The point of maximum coupling in k-space occurs at the point of minimum energy spacing between the two hybrid modes, marked by Ω in Figure 3. At this point, the hybrid modes are superpositions of the plasmon and C exciton states with equal weighting, however, as we detune away from this point to higher or lower k, the hybrid modes become more

plasmonic or excitonic. We can calculate the contribution of the plasmon and exciton to the hybrid modes throughout k-space by calculating the eigenvectors of the Hamiltonian in Equation (1). This is useful as it tells us where in k-space the coupling is appreciable, and therefore, how accurate we must be when probing strong coupling effects in this system. Furthermore, it allows us to spot any emergent exciton–exciton hybridization that may arise from simultaneously coupling the plasmon to multiple exciton modes, as we observed in our earlier work.[30]

We calculate the eigenvectors as follows. The new hybrid modes, $|\varphi\rangle_k$, may be written in the basis of the uncoupled modes according to Equation (2).

$$|\phi\rangle_k = c_1 |SPP\rangle + c_2 |A\rangle + c_3 |B\rangle + c_4 |C\rangle \qquad (2)$$

The Hopfield coefficients[33] $|c_n|^2$ represent the plasmonic and excitonic (A, B, or C) weighting of the hybrid modes, as a function of the wavevector. **Figure 4** plots the relevant coefficients for C exciton coupled modes (see Figure S4, Supporting Information, for all four coefficients).

The analysis shows the expected result that at the crossing point of the uncoupled modes of Figure 3, energy is equally distributed between the plasmon and the C exciton components. Away from this point, the ratio of the Hopfield coefficients $|c_4|^2/|c_1|^2$ falls to $1/e$ near $k_{//} = 0.0136$ and 0.0160 nm^{-1}. Thus, in this region of k-space, coupling effects are expected to be appreciable. In Figure S4, Supporting Information, we show that exciton–exciton hybridization is minimal in this system.

2.5. Discussion

The resulting best fit of the oscillator model and the experimentally observed values for the bare exciton energies and Rabi splitting values are summarized in **Table 1**. The difference between the experimental and fit values of the C exciton energy and Rabi splitting is ≤1%, indicating a good fit for the model in this region. The most important finding is that the Rabi splitting at the C exciton is 293 meV, which is $\eta = \frac{\Omega_C}{E_C} = 11\%$ of the uncoupled exciton energy. Compared to the ≈70 meV

Table 1. Best fit parameters from coupled oscillator model for strong coupling to the C exciton in MoS_2. Solved in k-space.

	E_A [eV]	E_B [eV]	E_C [eV]	Ω_A [meV]	Ω_B [meV]	Ω_C [meV]	$\eta = \frac{\Omega_C}{E_C}$
Experiment	1.86	2.01	2.67	58	77	296	11%
Model	1.86	2.01	2.59	67	95	293	11%

splittings at the A and B excitons in our similar systems,[30] this represents a factor of 2.4 increase in η, and enters the ultrastrong coupling regime ($\eta \gtrsim 10\%$), which is defined later.

We further note that the same oscillator analysis performed in θ-space (i.e., analyzing energy–θ_i rather than energy–k dispersion) yields a Rabi splitting fit of 532 meV which gives $\eta = 21\%$. The experimentally observed Rabi splitting in θ-space is 561 meV, which also gives $\eta = 21\%$ due to a slightly different fit value to the bare C exciton position (see Figures S5–S8 and Table S1, Supporting Information).

In the theory underlying strong coupling, the transition point from weak coupling (both modes at a single energy level) to strong coupling (two hybrid levels) occurs with a coupling strength, g, much lower than that required to observe Rabi splitting.[34] For small values of coupling strength (relative to the energy of the bare modes), the absence of Rabi splitting is generally assumed to be an uninteresting case as losses through the individual states should dominate any strong coupling effects. Hence, the commonly applied condition of strong coupling is $\Omega \geq (\gamma_{ex} + \gamma_{ph})/2$, where Ω is the observed Rabi splitting and γ_{ex} and γ_{ph} are the uncoupled exciton and photonic (e.g., cavity or plasmon modes) linewidths, respectively. In reality, this is a rule of thumb to help determine when strong coupling effects are large enough to be observable. Another rule of thumb is simply if Rabi splitting and anti-crossing are observable, then the modes are strongly coupled.[35] Furthermore, in this regime where Rabi splitting is observable, $\Omega \approx 2g$, and the terms Rabi splitting and coupling strength are nearly interchangeable. Ultrastrong coupling is defined for large values of coupling strength (relative to the energy of the bare modes), and unlike strong coupling, even in the absence of observable Rabi splitting due to lossy modes, interesting physics is still expected such as ground state virtual photons.[19] Thus, in the case of large observable Rabi splitting (i.e., within an order of magnitude of the bare mode energy, E), $\eta = \frac{\Omega}{E} \gtrsim 10\%$, the system is in both the strong and ultrastrong coupling regimes and associated physics are expected to be observable.

In our work, we meet both the strong and ultrastrong coupling definitions. To further quantify the strong coupling, we compare the average line widths of the uncoupled modes to the observed Rabi splitting. The width of the bare C exciton in k-space, $\gamma_{ex} = 220$ meV, is found by fitting the LP to a Lorentzian at large k, where mode is nearly completely excitonic. The fit to the bare plasmon at the point of coupling is $\gamma_{pl} = 99$ meV. This gives an average of $(\gamma_{ex} + \gamma_{pl})/2 = 160$ meV, much less than the measured splitting of $\Omega = 293$ meV. This can be seen directly in Figure 3 by visually comparing the average of the error bars representing the bare mode widths to the Rabi splitting Ω. Alternately, we may make this comparison in θ-space, that is, comparing to the raw data (see Figure S6, Supporting Information). The width of the bare exciton from fitting the absorption spectrum of Figure 1A is 510 meV, while the θ-space plasmon width is 406 meV, yielding an average line width of 458 meV. This is also considerably less than the experimentally observed θ-space Rabi splitting of 561 meV. We further note that the peak seen in Figure 1a at 415 nm, corresponding to the D exciton, does not strongly couple to the

plasmon as its width is far too large (see Supporting Information for further details).

One of the first papers demonstrating ultrastrong coupling in the visible spectrum used an organic J-aggregate dye molecule coupled to a plasmonic nanohole array to achieve 250 meV Rabi splitting at 1.8 eV transition energy, a ratio of $\eta = 14\%$.[11] Since then, η has reached as high as 60% in organic systems (e.g., J-aggregates, spiropyran, and squaraine) coupled to plasmonic or dielectric cavity modes.[12–14] In inorganic semiconductors, the ultrastrong coupling regime was first seen in the mid-infrared in 2009 by coupling microcavity modes to intersubband transitions (transition energy of ≈ 100 meV) in GaAs to achieve $\eta = 44\%$.[36] The only demonstration of ultrastrong coupling at optical frequencies in the TMDCs was in many-layer WS_2 at cryogenic temperatures; the Fabry–Perot resonance of a 32 nm flake was coupled to the A exciton to achieve 270 meV, or $\eta = 13\%$.[37] There are many other reports of $\eta = 4$–9% in the TMDCs.[4,38–44] All of these reports couple to the lowest energy A or B excitons. By targeting the larger oscillator strength of the C exciton, we achieve ultrastrong coupling at room temperature in the TMDCs.

Strong coupling results in shifted band positions or energy levels, which can lead to fundamentally new electronic and catalytic properties. There has been some work showing that chemical photoreaction pathways and rates can be manipulated by strongly coupling the reactants or catalysts with polariton modes.[45–49] However, studies using strongly coupled semiconductor electrodes in liquid electrolyte are lacking. This work uses the open "cavity" K–R configuration which makes such studies possible. Thus, ultrastrong coupling to the C exciton in TMDCs may find use in charge- or energy-transfer mediated photocatalytic chemical reactions, where the C exciton may have favorable energy and band-alignment for coupling to molecular orbitals of reactive species, intermediates, or products. Further applications specific to the C exciton in the TMDCs include slowed hot carrier cooling for enhanced conversion of solar energy into electricity or chemicals and enhanced SHG for coherent light sources in the violet/blue.

3. Conclusions

In summary, we find ultrastrong exciton–polariton coupling at the C exciton in FL-MoS_2, at room temperature. The observed Rabi splitting of 293 meV ($\eta = 11\%$) is significantly larger than that found in previous studies of the A and B excitons in TMDCs, due to the large C exciton oscillator strength. This degree of coupling, both in magnitude and as a fraction of the uncoupled energy, has largely been the domain of organic semiconductors. Our findings suggest that the C exciton of the TMDCs offers a route to ultrastrong coupling studies in CMOS-compatible inorganic semiconductors at room temperature. Further, the unique properties of the band-nested C exciton states, such as slowed hot exciton cooling, may be further enhanced through strong coupling, suggesting this system is a good candidate for hot-carrier studies toward controlling solar energy conversion to electrical or chemical potential.

**ADVANCED
SCIENCE NEWS**

www.advancedsciencenews.com

**ADVANCED
OPTICAL
MATERIALS**

www.advopticalmat.de

4. Experimental Section

Theoretical Calculations: The band structure of Figure 1b was calculated using ab initio density functional theory (DFT) methods to verify the band-nested structure in the 10 nm FL-MoS$_2$ samples. Although standard correlation functionals such as GGA–Perdew–Burke–Ernzerhof (PBE) used here tend to underestimate the band gap, the band profile was expected to remain accurate. In comparison to previous G0W0 calculations on mono-to-few layer (1–6) MoS$_2$,[50] it was found that the band profile remained similar. 16- and 17-layer structures were calculated to both span the 10 nm thickness of interest (calculated thicknesses of 9.7–10.3) and accounted for any even and odd layer dependence in the band structure.[51]

All calculations were performed using DFT with the JDFTx[52] software implementation. The PBE form of the generalized gradient approximation was used to describe the exchange–correlation interaction. The valence electron–nuclear interactions were described by optimized fully-relativistic norm-conserving Vanderbilt pseudopotentials (ONCVPSP)[53] from the PseudoDojo Project[54] (stringent accuracy). A 45 Hartree cut-off was used for the plane-wave basis set. Calculations were performed with fully-relativistic spin to capture the effects of spin–orbit coupling on the MoS$_2$ band structure. To capture the van der Waals interlayer interactions, the Grimme DFT + D2 scheme was used.[55]

The 16- and 17-layer MoS$_2$ slabs were constructed from lattice optimized bulk MoS$_2$. To prevent interaction between images, a vacuum layer of at least 15 Å was employed and truncated coulomb potentials[56] in the out-of-plane direction. The 2D multilayers were also allowed to fully relax to a final lattice parameter of 3.192 Å for both 16- and 17-layer structures and a final thickness of 9.7 and 10.3 nm, respectively. To sample the Brillouin zone, a Γ-centered k–point sampling of $12 \times 12 \times 3$ was used for the bulk and $12 \times 12 \times 1$ for the 2D multilayers. The convergence criteria were set to 1×10^{-6} Hartree for both structure and energy optimizations and converged via a variational minimization algorithm.[57] Finally, the density-of-states was obtained using the tetrahedron method for Brillouin zone integration.[58]

Prism Preparation: The right-angle prism used as a substrate was purchased from Edmund Optics (stock number 32–334), made from uncoated N-BK7 glass, with a 20 mm leg length. It was cleaned by sonicating in acetone and then isopropyl alcohol for several minutes, soaked in an aqua regia bath (3:1 hydrochloric acid:nitric acid) for an hour, rinsed twice with Milli-Q water, dried with a nitrogen spray gun, and further desiccated on a hot plate at 150 °C for several minutes. The cleaned prism was stored in a nitrogen dry box between cleaning and Ag deposition. Ag deposition was performed by electron beam deposition of ≈1 nm Ti followed by 40 nm of Ag, without breaking vacuum. The Ti serves as an adhesion layer but also damps the surface plasmon, so a minimum thickness was desired. The thickness of Ti/Ag was verified by profilometry and ellipsometry.

Few-Layer MoS$_2$ CVD Growth: The FL-MoS$_2$ growth procedures were adopted and modified from previous methods developed by Yu et al.[59] The CVD growth was carried out by a three-temperature-zone furnace. 500 mg of sulfur pellets (Sigma Aldrich) were placed at Zone 1, while the sapphire wafer (University Wafer) was located at Zone 3. An insert tube in Zone 2 was used to create an isolated local environment. 2 mg of MoO$_3$ powder (Sigma Aldrich) was loaded into the insert tube. 25 sccm Ar/O$_2$ (4 vol. % of O$_2$) premix gas flowed over the MoO$_3$ powder into Zone 2. The O$_2$ allows the MoO$_3$ precursor to remain in oxidized form as it was carried through the insert. 125 sccm of Ar was supplied at Zone 1 to carry the sulfur and balance the growth pressure at 1 Torr. During the growth, the temperatures in Zones 1, 2, and 3 were ramped at the rate of 35, 35, and 70 °C min^{-1} and then held for 30 min at 180, 530, and 930 °C, respectively. The thickness of MoS$_2$ was determined to be ≈10 nm by ellipsometry. The ellipsometry methods were previously verified against AFM and we further corroborated the few-layer thickness with Raman and PL on a film produced under the same growth conditions.[30]

MoS$_2$ Transfer: To transfer the CVD MoS$_2$ film onto the prism, the procedures described by Xu et al.[60] were followed. The CVD-grown MoS$_2$ was coated with polystyrene (PS, average molecular weight ≈192 000,

Sigma-Aldrich) dissolved in toluene (50 mg mL^{-1}) by spin-coating at 3000 rpm for 60 s. The resulting PS/MoS$_2$/sapphire film was dried in a 150 °C oven for 5 min. One edge of the film was scribed by a utility knife to create an opening for the etchant to access the MoS$_2$/sapphire interface. The substrate was soaked in 80 °C 2 M NaOH solution until the NaOH etched the interfacial sapphire across the wafer and the PS/MoS$_2$ film detached from the sapphire wafer. The PS/MoS$_2$ film was carefully transferred to ultra-pure water (18.2 MΩ) bath to minimize NaOH residue. Then, the PS/MoS$_2$ film, which naturally floats on the water surface, was transferred to the prism by lifting the prism from underneath the film. The PS coating was removed by soaking the prism in toluene. Finally, the prism was baked in N$_2$ at 300 °C for 30 min.

Transfer Matrix Simulations: The model was built in MATLAB[31] as NBK7 substrate / 1 nm Ti / 43 nm Ag / 0.27 nm Ag$_2$S / 8 nm MoS$_2$. The substrate refractive index and the thicknesses of Ag and MoS$_2$ were fit to reproduce the data. The NBK7 refractive index fit matched the specifications of Schott within ≈2%. The fit value for the MoS$_2$ thickness of 8 nm was near the value measured by ellipsometry of 10 nm. The refractive index for MoS$_2$ was measured from the top of the prism by ellipsometry and is shown in Figure S2a, Supporting Information. Refractive indices for Ag were modeled from ellipsometry data on witness samples and are in line with those of Palik[61] and Johnson and Christy[62] and the fit thickness was within 2 nm of that measured with ellipsometry. Refractive indices for Ti and Ag$_2$S were taken from refs. [63] and [64], respectively. The thickness of Ti was set to be 1 nm while the thickness of Ag$_2$S was derived from ellipsometry.

Supporting Information

Supporting Information is available from the Wiley Online Library or from the author.

Conflict of Interest

The authors declare no conflict of interest.

Data Availability Statement

The data that support the findings of this study are available from the corresponding author upon reasonable request.

**ADVANCED
SCIENCE NEWS**

www.advancedsciencenews.com

**ADVANCED
OPTICAL
MATERIALS**

www.advopticalmat.de

[1] Q. H. Wang, K. Kalantar-Zadeh, A. Kis, J. N. Coleman, M. S. Strano, *Nat. Nanotechnol.* **2012**, *7*, 699.

[2] Q. Lu, Y. Yu, Q. Ma, B. Chen, H. Zhang, *Adv. Mater.* **2016**, *28*, 1917.

[3] P. a. D. Gonçalves, N. Stenger, J. D. Cox, N. A. Mortensen, S. Xiao, *Adv. Opt. Mater.* **2020**, *8*, 1901473.

[4] J. Sun, Y. Li, H. Hu, W. Chen, D. Zheng, S. Zhang, H. Xu, *Nanoscale* **2021**, *13*, 4408.

[5] T. Byrnes, N. Y. Kim, Y. Yamamoto, *Nat. Phys.* **2014**, *10*, 803.

[6] H. Yokoyama, *Science* **1992**, *256*, 66.

[7] S. Christopoulos, G. B. H. von Högersthal, A. J. D. Grundy, P. G. Lagoudakis, A. V. Kavokin, J. J. Baumberg, G. Christmann, R. Butté, E. Feltin, J.-F. Carlin, N. Grandjean, *Phys. Rev. Lett.* **2007**, *98*, 126405.

[8] M. Waldherr, N. Lundt, M. Klaas, S. Betzold, M. Wurdack, V. Baumann, E. Estrecho, A. Nalitov, E. Cherotchenko, H. Cai, E. A. Ostrovskaya, A. V. Kavokin, S. Tongay, S. Klembt, S. Höfling, C. Schneider, *Nat. Commun.* **2018**, *9*, 3286.

[9] C. Anton-Solanas, M. Waldherr, M. Klaas, H. Suchomel, T. H. Harder, H. Cai, E. Sedov, S. Klembt, A. V. Kavokin, S. Tongay, K. Watanabe, T. Taniguchi, S. Höfling, C. Schneider, *Nat. Mater.* **2021**, *20*, 1233.

[10] J. Zhao, R. Su, A. Fieramosca, W. Zhao, W. Du, X. Liu, C. Diederichs, D. Sanvitto, T. C. H. Liew, Q. Xiong, *Nano Lett.* **2021**, *21*, 3331.

[11] J. Dintinger, S. Klein, F. Bustos, W. L. Barnes, T. W. Ebbesen, *Phys. Rev. B* **2005**, *71*, 035424.

[12] J. Bellessa, C. Symonds, K. Vynck, A. Lemaitre, A. Brioude, L. Beaur, J. C. Plenet, P. Viste, D. Felbacq, E. Cambril, P. Valvin, *Phys. Rev. B* **2009**, *80*, 033303.

[13] T. Schwartz, J. A. Hutchison, C. Genet, T. W. Ebbesen, *Phys. Rev. Lett.* **2011**, *106*, 196405.

[14] S. Gambino, M. Mazzeo, A. Genco, O. Di Stefano, S. Savasta, S. Patanè, D. Ballarini, F. Mangione, G. Lerario, D. Sanvitto, G. Gigli, *ACS Photonics* **2014**, *1*, 1042.

[15] C. A. DelPo, S.-U.-Z. Khan, K. H. Park, B. Kudisch, B. P. Rand, G. D. Scholes, *J. Phys. Chem. Lett.* **2021**, *12*, 9774.

[16] M. Held, A. Graf, Y. Zakharko, P. Chao, L. Tropf, M. C. Gather, J. Zaumseil, *Adv. Opt. Mater.* **2018**, *6*, 1700962.

[17] S. Kéna-Cohen, S. A. Maier, D. D. C. Bradley, *Adv. Opt. Mater.* **2013**, *1*, 827.

[18] B. Liu, M. Crescimanno, R. J. Twieg, K. D. Singer, *Adv. Opt. Mater.* **2019**, *7*, 1801682.

[19] S. De Liberato, *Nat. Commun.* **2017**, *8*, 1465.

[20] A. F. Kockum, A. Miranowicz, S. De Liberato, S. Savasta, F. Nori, *Nat. Rev. Phys.* **2019**, *1*, 19.

[21] A. Carvalho, R. M. Ribeiro, A. H. Castro Neto, *Phys. Rev. B* **2013**, *88*, 115205.

[22] D. Kozawa, R. Kumar, A. Carvalho, K. K. Amara, W. Zhao, S. Wang, M. Toh, R. M. Ribeiro, A. H. C. Neto, K. Matsuda, G. Eda, *Nat. Commun.* **2014**, *5*, 4543.

[23] L. Wang, Z. Wang, H.-Y. Wang, G. Grinblat, Y.-L. Huang, D. Wang, X.-H. Ye, X.-B. Li, Q. Bao, A.-S. Wee, S. A. Maier, Q.-D. Chen, M.-L. Zhong, C.-W. Qiu, H.-B. Sun, *Nat. Commun.* **2017**, *8*, 13906.

[24] Y. Li, J. Shi, H. Chen, Y. Mi, W. Du, X. Sui, C. Jiang, W. Liu, H. Xu, X. Liu, *Laser Photonics Rev.* **2019**, *13*, 1800270.

[25] A. H. Rose, T. J. Aubry, H. Zhang, D. Vigil-Fowler, J. van de Lagemaat, *J. Phys. Chem. C* **2022**, *126*, 8710.

[26] J. Shi, W.-Y. Liang, S. S. Raja, Y. Sang, X.-Q. Zhang, C.-A. Chen, Y. Wang, X. Yang, Y.-H. Lee, H. Ahn, S. Gwo, *Laser Photonics Rev.* **2018**, *12*, 1800188.

[27] T. Chervy, J. Xu, Y. Duan, C. Wang, L. Mager, M. Frerejean, J. A. W. Münninghoff, P. Tinnemans, J. A. Hutchison, C. Genet, A. E. Rowan, T. Rasing, T. W. Ebbesen, *Nano Lett.* **2016**, *16*, 7352.

[28] E. Drobnyh, R. Pachter, M. Sukharev, *J. Phys. Chem. C* **2019**, *123*, 6898.

[29] C. Symonds, C. Bonnand, J. C. Plenet, A. Bréhier, R. Parashkov, J. S. Lauret, E. Deleporte, J. Bellessa, *New J. Phys.* **2008**, *10*, 065017.

[30] A. H. Rose, J. R. Dunklin, H. Zhang, J. M. Merlo, J. van de Lagemaat, *ACS Photonics* **2020**, *7*, 1129.

[31] A. H. Rose, RTACalc 2 (MATLAB code), https://github.com/rose3fa/RTACalc, (accessed: February 2022).

[32] C. Cai, B. Zhang, X. Wang, L. Ling, T. Xu, T. Huang, H. Zhu, G. Bi, H. Wu, *EPL Europhys. Lett.* **2021**, *135*, 57001.

[33] J. J. Hopfield, *Phys. Rev.* **1958**, *112*, 1555.

[34] G. Khitrova, H. M. Gibbs, M. Kira, S. W. Koch, A. Scherer, *Nat. Phys.* **2006**, *2*, 81.

[35] P. Törmä, W. L. Barnes, *Rep. Prog. Phys.* **2015**, *78*, 013901.

[36] G. Günter, A. A. Anappara, J. Hees, A. Sell, G. Biasiol, L. Sorba, S. D. Liberato, C. Ciuti, A. Tredicucci, A. Leitenstorfer, R. Huber, *Nature* **2009**, *458*, 178.

[37] Q. Wang, L. Sun, B. Zhang, C. Chen, X. Shen, W. Lu, *Opt. Express* **2016**, *24*, 7151.

[38] S. Wang, S. Li, T. Chervy, A. Shalabney, S. Azzini, E. Orgiu, J. A. Hutchison, C. Genet, P. Samorì, T. W. Ebbesen, *Nano Lett.* **2016**, *16*, 4368.

[39] J. Wen, H. Wang, W. Wang, Z. Deng, C. Zhuang, Y. Zhang, F. Liu, J. She, J. Chen, H. Chen, S. Deng, N. Xu, *Nano Lett.* **2017**, *17*, 4689.

[40] M.-E. Kleemann, R. Chikkaraddy, E. M. Alexeev, D. Kos, C. Carnegie, W. Deacon, A. C. de Pury, C. Große, B. de Nijs, J. Mertens, A. I. Tartakovskii, J. J. Baumberg, *Nat. Commun.* **2017**, *8*, 1296.

[41] J. Cuadra, D. G. Baranov, M. Wersäll, R. Verre, T. J. Antosiewicz, T. Shegai, *Nano Lett.* **2018**, *18*, 1777.

[42] I. A. M. Al-Ani, K. As'Ham, L. Huang, A. E. Miroshnichenko, H. T. Hattori, *Laser Photonics Rev.* **2021**, *15*, 2100240.

[43] Y. Sang, C.-Y. Wang, S. S. Raja, C.-W. Cheng, C.-T. Huang, C.-A. Chen, X.-Q. Zhang, H. Ahn, C.-K. Shih, Y.-H. Lee, J. Shi, S. Gwo, *Nano Lett.* **2021**, *21*, 2596.

[44] M.-W. Yu, S. Ishii, S. Li, J.-R. Ku, J.-H. Yang, K.-L. Su, T. Taniguchi, T. Nagao, K.-P. Chen, *NPJ 2D Mater. Appl.* **2021**, *5*, 47.

[45] G. P. Wiederrecht, J. E. Hall, A. Bouhelier, *Phys. Rev. Lett.* **2007**, *98*, 083001.

[46] J. A. Hutchison, T. Schwartz, C. Genet, E. Devaux, T. W. Ebbesen, *Angew. Chem., Int. Ed.* **2012**, *51*, 1592.

[47] N. Azarova, A. J. Ferguson, J. van de Lagemaat, E. Rengnath, W. Park, J. C. Johnson, *J. Phys. Chem. Lett.* **2013**, *4*, 2658.

[48] A. Thomas, L. Lethuillier-Karl, K. Nagarajan, R. M. A. Vergauwe, J. George, T. Chervy, A. Shalabney, E. Devaux, C. Genet, J. Moran, T. W. Ebbesen, *Science* **2019**, *363*, 615.

[49] A. Mandal, T. D. Krauss, P. Huo, *J. Phys. Chem. B* **2020**, *124*, 6321.

[50] J.-Q. Hu, X.-H. Shi, S.-Q. Wu, K.-M. Ho, Z.-Z. Zhu, *Nanoscale Res. Lett.* **2019**, *14*, 288.

[51] Z. Wu, S. Xu, H. Lu, A. Khamoshi, G.-B. Liu, T. Han, Y. Wu, J. Lin, G. Long, Y. He, Y. Cai, Y. Yao, F. Zhang, N. Wang, *Nat. Commun.* **2016**, *7*, 12955.

[52] R. Sundararaman, K. Letchworth-Weaver, K. A. Schwarz, D. Gunceler, Y. Ozhabes, T. A. Arias, *SoftwareX* **2017**, *6*, 278.

[53] D. R. Hamann, *Phys. Rev. B* **2013**, *88*, 085117.

[54] M. J. van Setten, M. Giantomassi, E. Bousquet, M. J. Verstraete, D. R. Hamann, X. Gonze, G.-M. Rignanese, *Comput. Phys. Commun.* **2018**, *226*, 39.

[55] S. Grimme, *J. Comput. Chem.* **2006**, *27*, 1787.

[56] R. Sundararaman, T. A. Arias, *Phys. Rev. B* **2013**, *87*, 165122.

[57] T. A. Arias, M. C. Payne, J. D. Joannopoulos, *Phys. Rev. Lett.* **1992**, *69*, 1077.

[58] G. Lehmann, M. Taut, *Phys. Status Solidi B* **1972**, *54*, 469.

[59] H. Yu, M. Liao, W. Zhao, G. Liu, X. J. Zhou, Z. Wei, X. Xu, K. Liu, Z. Hu, K. Deng, S. Zhou, J.-A. Shi, L. Gu, C. Shen, T. Zhang, L. Du, L. Xie, J. Zhu, W. Chen, R. Yang, D. Shi, G. Zhang, *ACS Nano* **2017**, *11*, 12001.

[60] Z.-Q. Xu, Y. Zhang, S. Lin, C. Zheng, Y. L. Zhong, X. Xia, Z. Li, P. J. Sophia, M. S. Fuhrer, Y.-B. Cheng, Q. Bao, *ACS Nano* **2015**, *9*, 6178.

[61] D. W. Lynch, W. R. Hunter, in *Handbook of Optical Constants of Solids* (Ed.: E. D. Palik), Academic Press, Cambridge, MA **1985**, pp. 355–356.

[62] P. B. Johnson, R. W. Christy, *Phys. Rev. B* **1972**, *6*, 4370.

[63] D. W. Lynch, W. R. Hunter, in *Handbook of Optical Constants of Solids*, (Ed.: E. D. Palik), Academic Press, Cambridge, MA **1998**, pp. 245–247.

[64] J. M. Bennett, J. L. Stanford, E. J. Ashley, *J. Opt. Soc. Am.* **1970**, *60*, 224.

2200485 (8 of 8)